2019

A Compliant Microstructured Thermal Interface Material for Dry and Pluggable Interfaces

J. Cui
Purdue University

J. Wang
Purdue University

J. A. Weibel
Purdue University, jaweibel@purdue.edu

L. Pan
Purdue University

Cui, J.; Wang, J.; Weibel, J. A.; and Pan, L., "A Compliant Microstructured Thermal Interface Material for Dry and Pluggable Interfaces" (2019). *CTRC Research Publications.* Paper 356.
http://dx.doi.org/https://doi.org/10.1016/j.ijheatmasstransfer.2018.11.074

A Compliant Microstructured Thermal Interface Material for Dry and Pluggable Interfaces

Jin Cui[1], Jicheng Wang[1], Justin A. Weibel[1*], Liang Pan[1*]

School of Mechanical Engineering, Purdue University, West Lafayette, 47907, Indiana, USA

*Emails: jaweibel@purdue.edu and liangpan@purdue.edu

Abstract

Thermal interface materials (TIMs), such as thermal pastes and pads, can successfully enhance contact thermal conductance by filling the gaps caused by the surface nonflatness and roughness. However, there is still an unaddressed demand for TIMs which can be applied to pluggable or reworkable interfaces in electronic systems, such as in opto-electronic transceiver modules. Reducing the contact thermal resistances at these interfaces has become increasingly important as device power density increases. These applications require dry contact interfaces that can offer the required thermal conductance under a low pressure and endure repeated mechanical compression and shear. We present a compliant metallized finned zig zag micro-spring array, as a low-cost dry TIM, that allows conformal interface contact at low pressures (~10s to 100s of kPa) by effectively accommodating surface nonflatness at a rate of a few μm per kPa. Experimental characterization of the mechanical compliance and thermal resistance confirm that this dry TIM can achieve conformal thermal contact between nonflat mating surfaces under low pressures. The total insertion thermal resistance of this dry TIM, even when mating to nonflat surfaces, is comparable to that of a polished and flat metal-to-metal contact. Mechanical compression and shear cycling tests are performed to assess the durability.

Keywords: Dry contact, Thermal interface material, Compliant micro-springs, Projection micro-stereolithography, Metallization, Mechanical durability, Sliding contact

1. Introduction

The increasing power density of electronic devices calls for the development of novel thermal solutions that can reduce the interfacial contact thermal resistances in the path of heat rejection [1-4]. Interface resistance can primarily be attributed to gaps between mating surfaces caused by micro-scale surface asperities (roughness) and wavy surface profiles (nonflatness) [5-7]. Contact thermal resistance can be reduced by applying high compressive pressures to mechanically deform the surfaces and increase interfacial contact area. However, pressures of ~1 to 100s MPa, at least, are required to effectively reduce contact thermal resistance for metal-to-metal interfaces [8-10]. An effective solution to reduce contact thermal resistance without using high pressures is to fill the gaps with wet thermal interface materials (TIMs), such as flowable greases and pastes or soft gel pads [4]. As an alternative to these wet TIMs, there is extensive work [11-13] using micro- and nano-structured materials to engineer high-performance, compliant thermal interfaces. Particle-laden polymers (PLPs) [14-17] have compliant characteristics from the polymer matrix, while the filler nano- and micro-particles of high thermal conductivities enhance the thermal conductivity of the polymer matrix. Higher ratio of filler particles leads to better thermal conductivity, but with the cost of mechanical compliance [13]. Vertically aligned carbon nanotubes (CNTs) have extremely high axial thermal conductivity [18, 19], which can be bonded to the mating surfaces to

enhance contact thermal conductance [20, 21]. Compliant metallic nano-springs [22, 23] and nanowires [24,25] can be easily deformed and conformally soldered onto a rough surface. These micro- and nano-structured TIMs provide viable solutions that significantly enhance interfacial thermal conductance for surfaces with microscopic roughness, however, these TIMs bond surfaces permanently or deform plasticly to achieve conformal contact with the mating surfaces, which are designed for applications where the mating surfaces do not move across each other. There is an unaddressed demand for dry contact interface materials in applications that require surfaces to repeatedly slide into contact with a mating heatsink, such as in pluggable opto-electronic transceiver modules [26]. In these pluggable applications, although the roughness of mating surfaces can be easily polished to be very smooth, the nonflatness remains nontrivially large, due to the size of the surfaces and cost/accuracy constraint of the manufacturing process. Dry and pluggable TIM solutions are required to accommodate a surface nonflatness at 10s of μm in these electronic applications. We have recently demonstrated metallized soft microstructures have the potential to be a dry TIM solution that increases the interfacial contact area and conforms to nonflat surfaces under low pressures [27, 28].

Here, we report a new dry TIM made of metallized finned zig zag micro-springs that conforms to highly nonflat surfaces under low pressures, as required for pluggable thermal interface applications. The high mechanical compliance is structurally achieved by using the zig zag microscale springs that can easily deform under low pressures, with symmetric deformation to maintain in consistent contact with the mating surface. The high thermal conductance is achieved by metallizing the springs to form highly conductive thermal pathways. Microscale fins are added to the rigid portion of the spring structure, such that there is a significant increase in the surface area for metallization without reducing the compliance. This new dry TIM can be directly fabricated onto the device or heatsink surfaces to provide an enhanced interfacial conductance. We measure the insertion thermal resistance of this dry TIM and demonstrate that it provides significantly improved thermal conductance compared to that of metal-to-metal contact for nonflat interfaces under low pressures. Mechanical cycling tests are conducted to confirm the early-stage durability of the micro-springs.

2. Methods and Materials

2.1. Microstructured TIM Design

As shown in Figure 1(a) and 1(b), the thermal interface material (TIM) consists of an array of micro-springs and a base layer underneath. The micro-spring geometry is designed to deform under low pressures and conformally contact a nonflat surface, which would significantly increase the interfacial contact area compared to bare metal-to-metal contact of nonflat surfaces. Each element in the array is a so-called “finned zig zag micro-spring,” as shown in Figure 1(c), 1(d) and 1(e). Each micro-spring has a footprint size of 700 μm ×580 μm and a height of 440 μm, consisting of two zig zag springs connect at the top by a slotted plate; a series of thin fin plates are located on the side walls of the springs. The two zig zag springs arranged back-to-back and connected in this manner to form a symmetrical structure, which can avoid tilting of the top plate and ensure contact with the mating surface when compressed. The entire external surface of the micro-springs is coated by a thin metal layer to enhance their thermal conductance. The fins dramatically increase surface area for attachment of the metal layer, and thereby the metal cross sectional area, to

enhance thermal conductance of the micro-springs. The slots in the top surface anchor the metal layer and also provide a thermal pathway through this feature. A total of 70 finned zig zag micro-springs form a 7 × 10 array. The gap between two neighboring micro-springs is 200 μm. The base layer is designed under the micro-spring array for convenience of handling and transfer. The thickness of base layer is 200 μm.

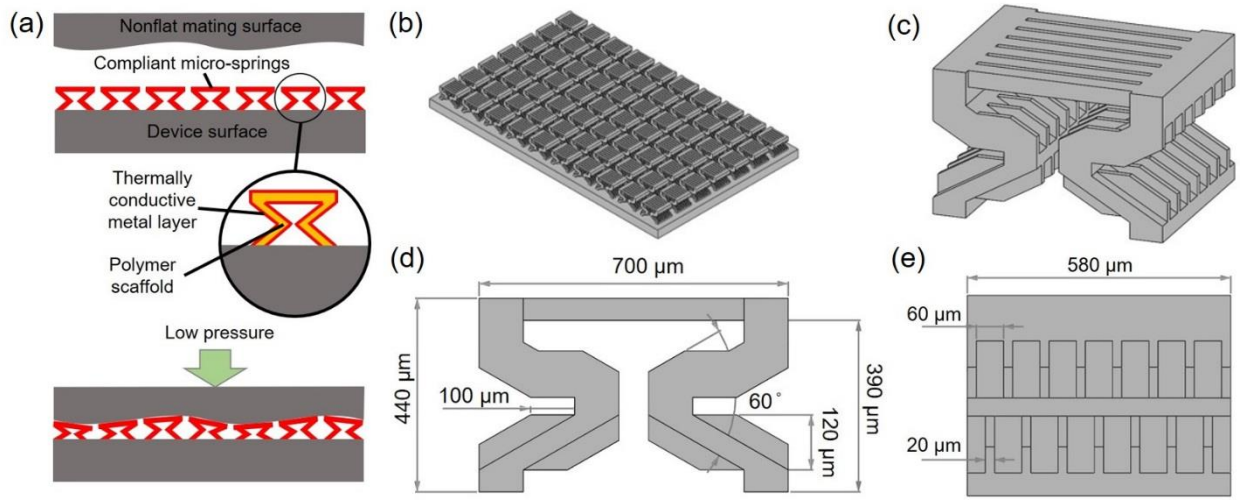

Figure 1. (a) Working mechanism of a microstructured thermal interface material (TIM) made of compliant micro-springs that conformally contacts with a nonflat mating surface at a low pressure. (b) Isometric view of three-dimensional (3D) model of the TIM consisting of an array of finned zig zag micro-springs; (c) Dimetric, (d) front, and (e) side views of the 3D model of an individual finned zig zag micro-spring.

2.2. Fabrication of Polymer Scaffolds

Projection-type micro-stereolithography (μSL) is a scalable and cost-effective technology to fabricate three-dimensional (3D) microstructures for various applications in microfluidics, photonics, and metamaterials [29-32]. In this work, a custom-constructed projection-type μSL system is used to fabricate the polymer scaffolds, which can build 3D structures at a speed of ~10 to 100 μm/s.

Before fabrication, a 3D model of the structure is created and sliced at a specified layer thickness to generate a series of two-dimensional (2D) cross-sectional images, which are rendered on the programmable digital micromirror device (DMD) one by one during fabrication process. As schematically shown in Figure 2, the 3D structure is built onto a flat silicon substrate that is initially covered by a thin layer of photocurable resin liquid. This thin liquid layer serves as the build layer, with a thickness controlled to be equal to the sliced layer thickness. At each build step, UV light irradiates on the DMD, which reflects one 2D image onto the resin surface to photocure the top build layer of the resin. After polymerization of the exposed build layer, the UV irradiation is switched off and the mechanical stage moved downward to allow a fresh layer of uncured resin liquid to flow in and cover the previously solidified layer. Meanwhile, the DMD image changes to the next pattern, and then the process cycle of irradiation, polymerization, and recoating repeats

until the entire 3D structure is fabricated. By using this projection scheme, the entire layer can be polymerized at one exposure, which enables faster build speed and less stitching error compared to other 3D microfabrication technologies which use point-wise scanning schemes [33, 34]. The fabrication resolution is less than 10 μm, which is sufficient to define the finest feature (fin thickness 20 μm) of the finned zig zag micro-spring array (as shown in Figure 1).

Several types of of photocurable resins are compatible with the projection μSL system. For the structures fabricated in this study, we use a mixture of polyethylene glycol diacrylate (PEGDA, Sigma-Aldrich), 0.5 wt% photoinitiator (Irgacure 918, Ciba), and 0.2 wt% photoabsorber (Sudan I, Sigma-Aldrich). A 1 wt% sensitization solution (see section 2.3 for details) is mixed with the resin as the sensitization agent for the later metallization process. Under the irradiation of UV light (405 nm), the photoinitiator generates radicals to trigger the polymerization of PEGDA monomers. The photoabsorber limits the penetration depth of UV light into the resin bath to control the cured layer thickness.

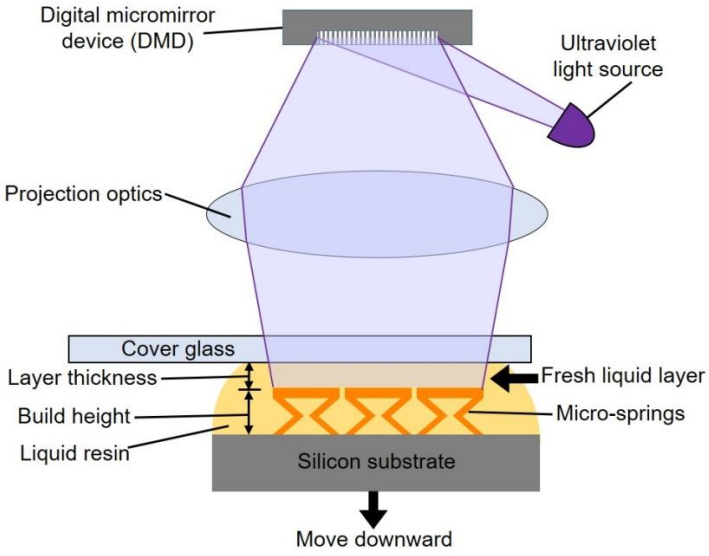

Figure 2. Schematic diagram of the projection micro-stereolithography (μSL) system which utilizes ultraviolet (UV) light to build polymer scaffolds in photocurable resin layer by layer.

2.3. Metallization

The polymer scaffold is metallized in two sequential steps: electroless plating of a 2-μm thick layer of copper followed by electroless plating of a 0.5-μm thick layer of nickel [35, 36]. The thick copper layer provides a thermal conduction pathway and the thin nickel layer serves as a hard overcoat to protect the copper layer from oxidation and potential mechanical damage. Conventional procedures for electroless plating on polymers require surface etching to create small holes in order to grow an attached metal layer. The etching process compromises accuracy in the shape and size of structures and damages small features. We developed a new activation process to avoid the need for surface etching. Before fabrication of the polymer scaffolds, the 1 wt%

sensitization solution (aqueous tin(II) chloride solution at 10 wt%) is mixed with the photocurable resin. By soaking the fabricated polymer scaffolds in an activation solution (0.025 wt% palladium chloride solution), the nucleation reaction occurs at the interface and generates metal particles as catalyst for metallization on the surfaces of polymer scaffolds, which allows the metal layer to directly grow onto the polymer. This etching-free activation process is critical to preserve the small fin structures. After activation, the polymer scaffolds are rinsed and plated in a plating solution consisting of 0.45 wt% copper sulfate ($CuSO_4$) with 1 wt% formaldehyde (CH_2O) as a reducing agent and 2 wt% potassium sodium tartrate ($KNaC_4H_4O_6$) as a complexant. The pH value of solution is adjusted to be remain in the range of ~9 to 10 using 0.4 wt% sodium hydroxide (NaOH). For electroless nickel plating, the plating solution consists of 3 wt% nickel sulfate ($NiSO_4$) solution with 2 wt% sodium hypophosphite (NaH_2PO_2) as a reducing agent and 1.7 wt% sodium malate as a complexant. The pH value of the nickel plating solution is adjusted to stay in the range of ~4 to 5 by adding acetic acid. After metallization, the top surface of the metallized TIM is gently hand wiped using a soft cloth with metal polishing compound to remove large particles and asperities.

2.4. Mechanical Compliance and Sliding Contact Characterization

The experimental setup shown in Figure 3(a) is used to characterize the mechanical compliance of the TIM under a normal pressure. A TIM sample is placed between two flat, rigid plates which are placed on a three-axis translation stage. The TIM is compressed by using a loading platform via an axial shaft which passes through a fixed linear bearing. A spring is placed between the linear bearing and loading platform to offset the dead-load from the platform. A ball bearing directly contacts the top plate to ensure that all force is applied normal to the sample plate without any shear. The force applied to sample is measured using a load cell (Omega LCFD-1kg; ± 0.015 N) placed in line with the axis of the shaft. The deformation of the TIM sample is measured optically from the side view using a digital camera and a high-magnification zoom lens (VH-Z50L, Keyence). During measurement of the mechanical compliance, the pressure applied to the TIM is successively increased and decreased in small increments; this loading and unloading processes is repeated multiple times to evaluate hysteresis in the sample deformation.

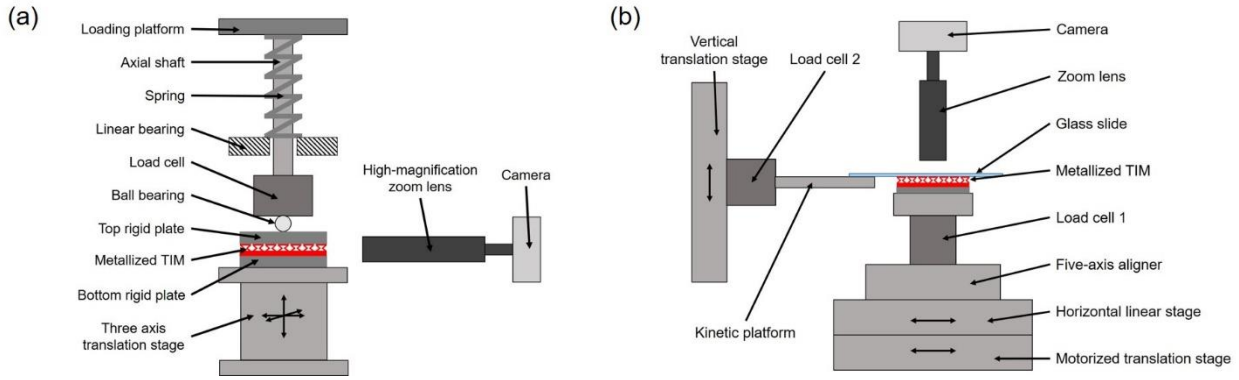

Figure 3. Schematic diagram of the experimental setups used to (a) characterize the mechanical compliance of the TIM and to (b) observe the deformation of metallized TIM sliding against a glass slide and characterize shear and normal force during sliding.

Using the experimental setup shown in Figure 3b, we observe behavior of the metallized TIM under a sliding contact and characterize the shear force for an applied normal pressure. The TIM is fixed on a horizontal platform. The load cell underneath the platform (load cell 1) is used to measure the normal force applied on the TIM. A stack of manual alignment stages (a five-axis aligner and a translational stage) and a motorized translational stage are placed underneath this to adjust and control the position and motion of the TIM platform. The metallized TIM is compressed from above against a fixed and flat glass slide; the vertical position of the glass slide is adjusted using a linear stage to control the normal force. The motorized translational stage is used to actuate the compressed TIM structure to slide against the glass surface at a set speed. Ensuring the parallelism between the glass slide and TIM is essential to maintain a constant normal force during the sliding contact test. A load cell connected to the kinetic platform (load cell 2) is used to measure the shear force during the test.

2.5 Thermal Resistance Measurement

An experimental setup is designed to characterize the thermal resistance of the TIM, as schematically shown in Figure 4(a). The TIM is sandwiched between two aluminum (6061, thermal conductivity 150 $W \cdot m^{-1} \cdot K^{-1}$) bars which have the same cross-sectional area as the TIM and provide the heat conduction path for the measurement. A resistance heater is attached to the top of the upper aluminum bar as the heat source, and a pin-fin heatsink is attached under the lower bar to remove heat from the bottom. Thermal insulation (PEEK, thermal conductivity ~0.3 $W/m^{-1} \cdot K^{-1}$) is applied around the heat path to ensure one-dimensional heat conduction. Five thermocouples (Omega T-type, ±0.2℃) are used to measure temperatures at preset positions (±0.5 mm) along the center of the aluminum bars. The heat flux and bottom temperature of the TIM interface are determined based on the temperature gradient measured by the four thermocouples in the lower bar. The thermocouple in the upper bar is used to obtain the temperature on the top interface of the TIM by extrapolation. The total insertion thermal resistance of the TIM is calculated based on the total temperature difference across the TIM and heat flux through the bars.

As shown in Figure 4b, the total insertion thermal resistance consists of four components: contact resistance between the micro-springs and mating surface ($R_{c,top}$), resistance of the micro-springs (R_s), resistance of the base layer (R_b), and contact resistance between base layer and contact surface ($R_{c,bot}$). The effective thermal resistance (R_{eff}) of the TIM consists of R_s and $R_{c,top}$, while R_b and $R_{c,bot}$ are determined by the choice of the base layer and attachment method.

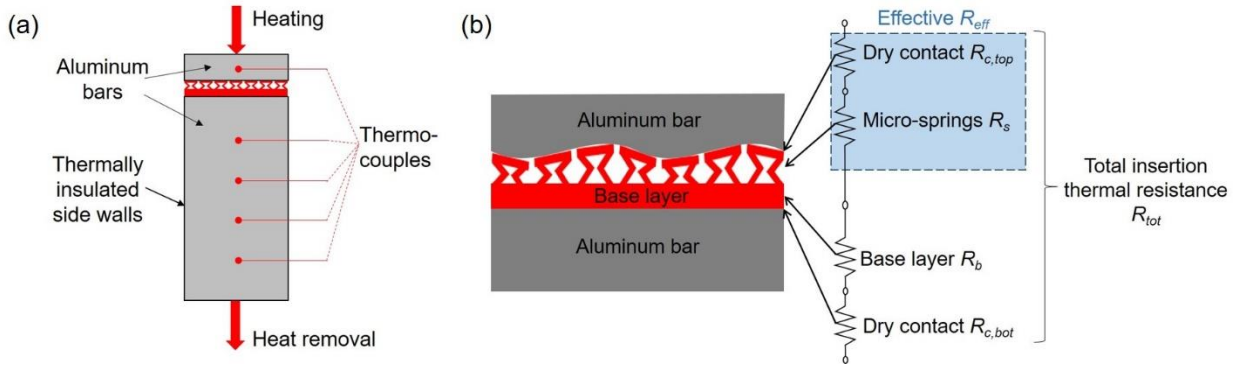

Figure 4. (a) Schematic diagram of the experimental setup to characterize the thermal resistances of the TIM; (b) illustration of the component resistances contributing to the total insertion thermal resistance measured in the test facility.

3. Results and Discussion

3.1. Metallized Finned Zig Zag Micro-Spring Array

Microscopic images of the finned zig zag micro-spring array are shown at different fabrication stages in Figure 5. From the top view image of the polymer scaffold structures shown in Figure 5(a), all of the micro-springs are observed to be fabricated with good uniformity across the whole fabrication area without defects. Figure 5(b) shows a top view image of the TIM immediately after metallization. The cross section of the metallized TIM is observed under a high-magnification microscope to examine the thickness of metal layer. The metallized TIM has a uniform metal layer of ~2.5 μm, which is made of ~2 μm thick copper layer and ~0.5 μm thick nickel layer above the copper layer. A magnified top view image of the metallized TIM is shown in Figure 5(d), which reveals the rough top surface (surface roughness of ~1 μm as measured using an optical surface profiler). After polishing, for the TIM as shown in Figure 5(c) and Figure 5(e), the surface roughness of the top surface is reduced to ~0.3 μm. Figure 5(f) and Figure 5(g) show scanning electron microscopic (SEM) images of an individual metallized micro-spring after polishing, which has the shape and dimensions as designed. The fins are fabricated properly at a thickness of ~20 μm. The textures on the side wall of the micro-spring reveal the intrinsic property of layer-by-layer fabrication with a layer thickness of ~10 μm.

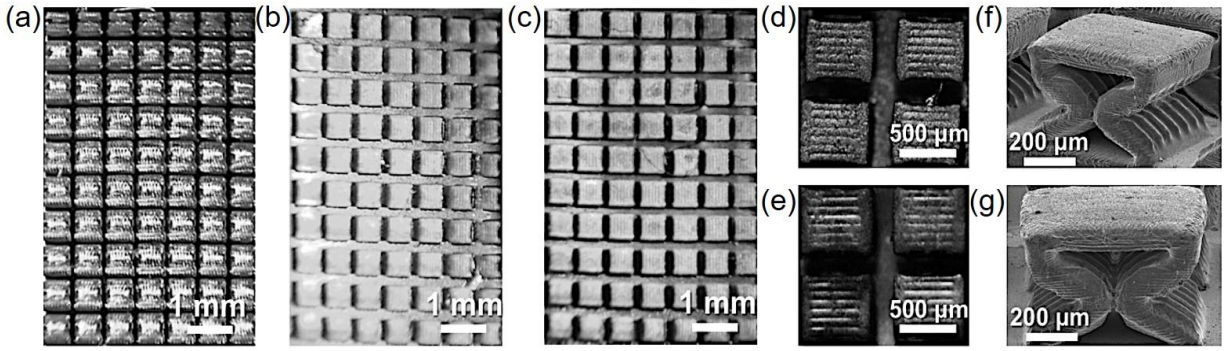

Figure 5. Microscopic images of the micro-spring array at different fabrication stages: (a) top view of the polymer scaffold, top view of a metallized TIM (b) before and (c) after polishing and magnified top view of four micro-springs (d) before and (e) after polishing. Scanning electron microscopic (SEM) images of (f) dimetric and (g) front view of an individual metallized micro-spring after polishing.

3.2. Effective Thermal Resistance (R_{eff})

The effective thermal resistance (R_{eff}) of the TIM is characterized at a compression of 20 kPa at three different stages of the fabrication process: the polymer scaffold, after metallization, and after surface polishing. The mating surface used here is a nominally flat surface after standard machining and fine surface polishing. The surface profile of the flat surface is shown in Figure 6(a), as characterized by an interferometer; the surface is generally flat but has some deep scratches that cannot be removed by hand polishing. To obtain R_{eff}, the base layer resistance R_b and bottom contact resistance $R_{c,bot}$ were subtracted from the measured total insertion thermal resistances of the TIM. The values of R_b and $R_{c,bot}$ are measured at the same pressure of 20 kPa based on several experimental measurements of thermal resistances when solid polymer blocks of different thickness are inserted between the bars separately [28]. Figure 6(b) shows the effective thermal resistance of the TIM at the three different processing stages, which reveal that metallization and surface polishing significantly decrease the thermal resistance of the structure. The polymer scaffold has the highest R_{eff} (3080 ± 120 mm^2·K/W), which is substantially decreased after the metallization to 600 ± 50 mm^2·K/W. After surface polishing, R_{eff} further decreases to 280 ± 40 mm^2·K/W.

To further evaluate the thermal resistance of the TIM mating with a nonflat surface, the upper aluminum bar is laser-etched to impart a controlled nonflatness. The laser-machined texture consists of a series of periodic steps alternating between 0.5-mm wide plateaus and 2-mm wide grooves; the step change in height between the plateaus and grooves is ~10 µm. After laser machining, the surface is polished and cleaned to remove particles and asperities. The surface profile of the nonflat surface is shown in Figure 6(c); the periodic lines in the etched area are artifacts of the scanning trajectory of the laser. We compare the effective thermal resistances (R_{eff}) of the TIM (after all fabrication steps) to that of the direct metal-to-metal contact in Figure 6(d). The direct metal-to-metal contact has thermal resistances of 320 and 1650 mm^2·K/W, for the flat

and nonflat mating surfaces, respectively. The thermal resistance increases by over 5 times due to the dramatic contact area reduction. Conversely, the effective thermal resistances of TIM are 280 and 300 $mm^2 \cdot K/W$, for flat and nonflat mating surfaces, respectively, a difference smaller than the measurement uncertainty. This result confirms that effective thermal resistance of the TIM is nearly independent of the degree of surface nonflatness. We note that for the polished flat surface, the magnitude of the effective resistance of the TIM is even lower than that of direct metal-to-metal contact, likely due to the presence of slight nonflatness incurred by polishing the nominally flat surface. Although the tests shown here were conducted using a surface with 5 μm nonflatness, the metallized TIM is expected to performs similarly for a larger nonflatness values, as long as the pressure is sufficient to deform the micro-spring array into conformal contact with the mating surface. Note that our thermal tests are performed with the TIM at an absolute temperature of 20-50˚C, representative of many typical application environments. The highest viable operating temperature of the TIM would be limited by the glass transition temperature of the polymer scaffold material at ~180˚C.

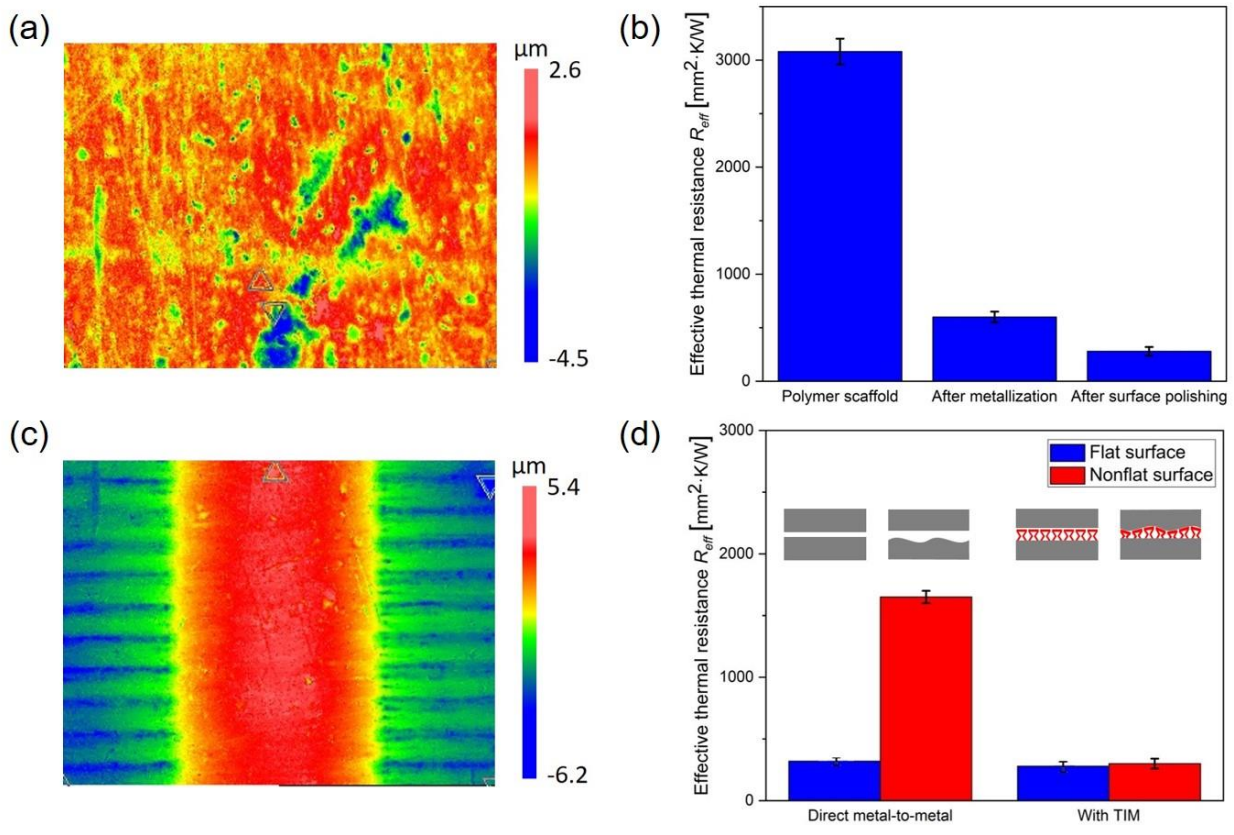

Figure 6. Surface profiles of the (a) flat and (c) nonflat mating surfaces over an area of 1.4 mm × 1 mm. (b) Effective thermal resistances of the TIM (mating with a flat, polished surface) at three different fabrication stages: polymer scaffold, after metallization, and after surface polishing. (d)

Comparison of the thermal resistance of a dry metal-to-metal interface, with and without the fully fabricated TIM inserted, for flat and nonflat polished mating surfaces.

3.3. Total Insertion Thermal Resistance

Fabricating the TIM directly onto the working surface will provide the lowest insertion resistance, equivalent to the effective thermal resistance, by eliminating both R_b and $R_{c,bot}$, as illustrated in Fig. 4. In some applications, creating a polymer base can provide the advantages for handling as a standalone material or integration convenience, at the toll of an increased insertion resistance.

The base thermal resistances (R_b) introduced by the base layer can be relatively very large for moderate base thicknesses, due to the low thermal conductivity of polymer. The bottom interfacial thermal resistance ($R_{c,bot}$) between the polymer base and mount surface can also be large if not addressed. Even if the effective thermal resistance of the TIM is low, the TIM may still lose its application advantages if R_b and $R_{c,bot}$ cannot be sufficiently lower than R_{eff}.

To demonstrate an integration strategy for reducing R_b and $R_{c,bot}$, we fabricate a base layer of 200 μm with through-holes (100 μm × 580 μm) near the feet of the micro-springs. The inner surfaces of the through-holes are coated with highly conductive metals during the metallization process, therefore effectively reducing the overall R_b by providing low-resistance pathways for heat diffusion that bypass the polymer base. Furthermore, the base layer is attached to the mounting surface using a thin layer of epoxy (<10 μm) to reduce $R_{c,bot}$. During this fabrication step, the through-holes in the base also allow for excess epoxy to readily squeeze out from the interface, for reliable formation of a thin epoxy layer.

The total insertion thermal resistances of the TIM are measured for a flat, polished mating surface at 20 kPa in the three scenarios illustrated in Fig. 7(a): direct dry contact between the solid base layer and mount surface, attachment of the solid base layer using a thin layer of epoxy, and attachment of a base layer with conducting through-holes using epoxy. The total insertion thermal resistance of TIM with a solid polymer base layer in direct dry contact with the device surface is 1120 ± 30 $mm^2 \cdot K/W$, as shown in Fig. 7(b). Using the same solid base layer, the total insertion resistance of the TIM is reduced to 560 ± 15 $mm^2 \cdot K/W$ by attaching with a thin layer of epoxy. By adding the conducting through-holes to the base, the resistance is further reduced to 350 ± 10 $mm^2 \cdot K/W$, which is comparable to the thermal resistance of direct metal-to-metal contact between polished and flat surfaces (320 $mm^2 \cdot K/W$). The resistance reductions obtained by attaching with epoxy and inserting conducting through-holes are 560 $mm^2 \cdot K/W$ (Δ_1) and 210 $mm^2 \cdot K/W$ (Δ_2), respectively.

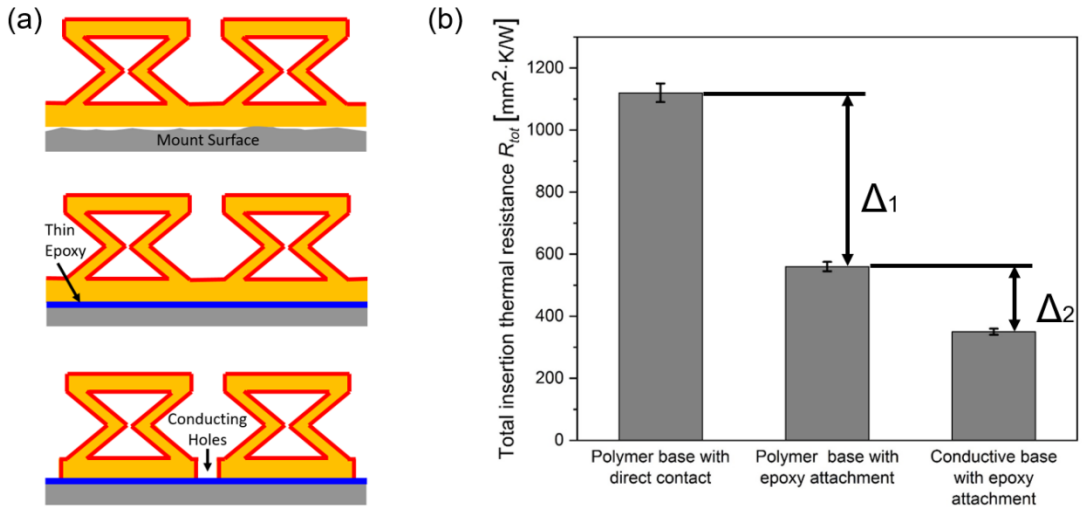

Figure 7. (a) Illustrations of three insertion scenarios: which are direct dry contact between the solid base layer and mount surface, attachment of the solid base layer using a thin layer of epoxy, and attachment of a base layer with conducting through-holes using epoxy. (b) Measured insertion thermal resistances (flat surface, 20 for the three scenarios where Δ_1 indicates the resistance reduction by attaching with a thin layer of epoxy and Δ_2 indicates the compounding resistance reduction by adding the thermally conducting through-holes.

3.4. Mechanical Compliance and Durability under Normal (Compression) Pressure

The mechanical compliance of the metallized TIM is evaluated by applying increasing pressures up to 40 kPa. Figure 8(a) plots the vertical displacement of the top surfaces of the micro-springs as a function of the applied pressures for two loading and unloading cycles. The metallized TIM fully recovers to its original height and exhibits no obvious hysteresis after two cycles. The displacement with pressure has good linearity; the mechanical compliance of the metallized TIM is extracted from the data using a linear fit and measured to be 2.35 μm/kPa. The TIM was compressed to a higher pressure of 200 kPa without damage; at a pressure higher than 250 kPa, corresponding to a maximum vertical deflection of ~100 μm, the TIM starts to show signs of damage. The achievable deformation of the TIM at this pressure is sufficiently large to accommodate the surface nonflatness for most electronic packaging applications. During the compression process, the top surface of the finned zig zag micro-spring was observed to stay in consistent contact with the mating surface, as shown in insets of Figure 8 (a).

The durability of the metallized TIM was investigated by applying a 20 kPa normal pressure for 100 loading and unloading cycles. The chosen pressure and number of cycles are typical values to emulate application requirements for pluggable opto-electronic transceiver modules. Figure 8(b) shows effective thermal resistance for a polished flat surface at 20 kPa normal pressure before and after cycling, which are almost unchanged (the difference is within measurement uncertainty). As shown in Figure 8(c), the mechanical compliance remains nearly constant during cycling. Figure 8(d) shows the vertical displacements of the top surface of the TIM after each loading and

unloading cycle. The difference between the loading and unloading displacement curves indicates the elastic deformation of the TIM which remain nearly constant within the first 100 cycles. In the initial 20 cycles, the metallized TIM undergoes a plastic deformation of ~12 μm which is ~25% of the overall elastic deformation. After 20 cycles, the TIM deforms elastically. These results confirm that the thermos-mechanical performance of the metallized TIM is stable in the early stage of usage under a low compressive pressure of 10s of kPa.

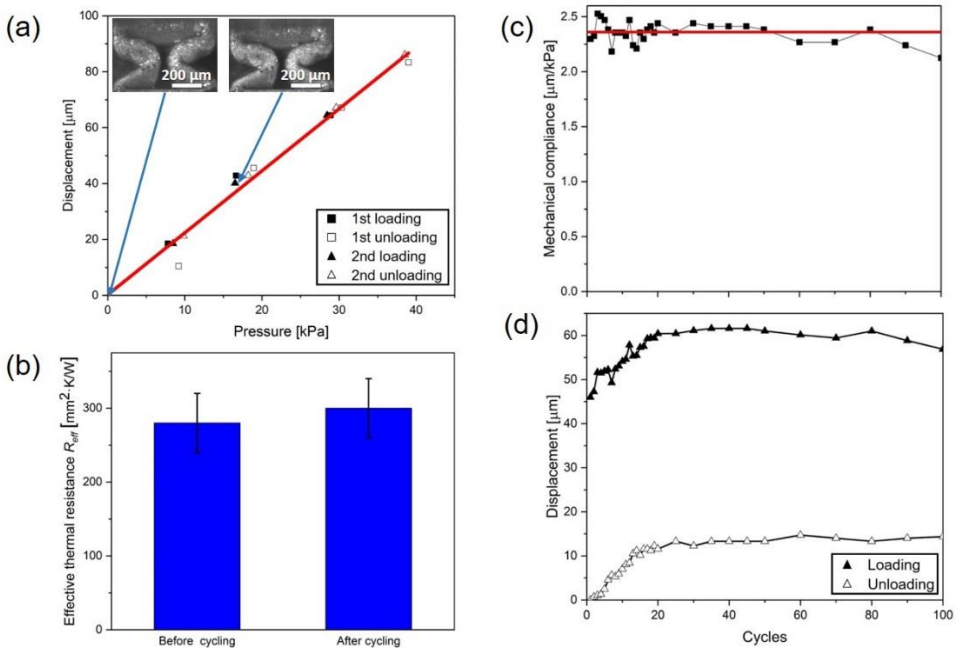

Figure 8. (a) Characterization of the vertical displacement as a function of the applied pressure of the metallized TIM. The solid line is the linear fit of the data with a slope indicating the mechanical compliance. The insets are microscopic images of a micro-spring under normal pressures of 0 and 20 kPa. At 20 kPa, the micro-spring is compressed, and the top surface stays in contact with the mating surface during compression. (b) Effective thermal resistance of the metallized TIM for a polished flat surface at 20 kPa normal pressure before and after 100 cycles. (c) Mechanical compliance of the TIM during normal cycling at 20 kPa, the red horizontal line indicates the average of measured mechanical compliance (2.35 μm/kPa). (d) Vertical displacement of the top surface of the metallized TIM after loading and unloading during cycling.

3.5. Characterization under Sliding Contact

In the sliding contact measurement, the metallized TIM was pressed against the glass slide at ~20 kPa and moved laterally at a speed of 5 mm/s over a distance of 5 mm, to characterize its robustness under shear. Figure 9(a) shows the measured normal force TIM (solid triangles) and shear force (solid circle) applied to the metallized TIM during sliding contact. During sliding, both the normal and shear forces remain almost constant. The average normal force is 1.21 N, which corresponds to the preset compression pressure of 20 kPa. The average shear force is 0.41 N, corresponding to

a friction coefficient of ~0.3. To assess the robustness under cycled shear loading, we continuously slide the metallized TIM back and forth 100 times. Within these 100 cycles, there is were significant changes in measured normal and shear forces. As shown in Figure 9(b), the effective thermal resistance of the metallized TIM for a polished flat surface at 20 kPa normal pressure before and after 100 sliding cycles is almost unchanged (difference within measurement uncertainty). No obvious structural damage is detected after 100 sliding cycles.

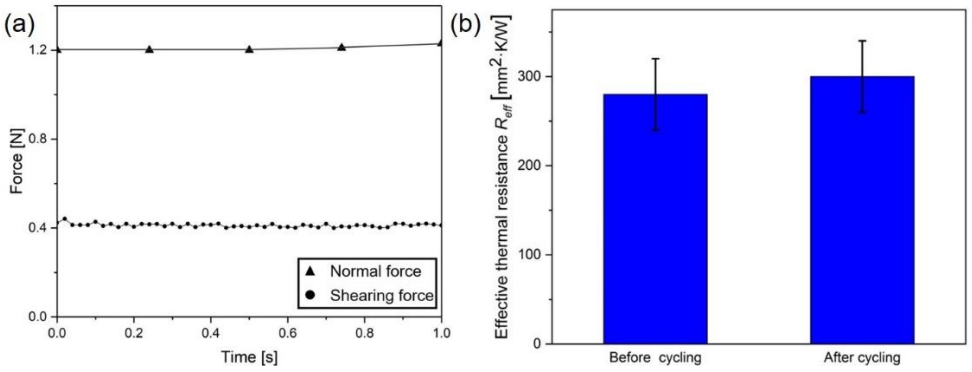

Figure 9. (a) Normal and shear force on the metallized TIM measured during sliding against a glass slide under 20 kPa compressive pressure. (b) Effective thermal resistance of the metallized TIM for a polished flat surface at 20 kPa normal pressure before and after 100 sliding cycles.

4. Conclusions

We demonstrate a metallized micro-spring array as a thermal interface material (TIM) to enhance dry contact thermal conductance across nonflat interfaces under low pressures of a few to a few hundreds of kPa. A symmetric finned zig zag micro-spring geometry is designed to enhance the contact area under compression. Projection micro-stereolithography (μSL) is used to create the compliant polymer scaffold. An electroless metal plating method, with etching-free activation, is used to coat the polymer scaffold with metal to improve the thermal conductance of the micro-spring array. The effective resistance of this metallized TIM is measured to be 280 ± 40 mm^2·K/W. Thermal resistances tests conducted for both flat and nonflat mating surfaces confirm the effective thermal resistance of the TIM is nearly unaffected by surface nonflatness and significantly outperforms direct metal-to-metal contact between nonflat surfaces. Mechanical cycling tests under normal pressure and sliding contact confirm the early-stage durability of the metallized TIM. In addition to fabricating directly it onto a working surface, an insertion approach is demonstrated for which the metallized TIM can be fabricated with a conductive base layer and used as an attachable TIM that is affixed to the surface. This dry TIM is fabricated using scalable techniques compatible with high-volume production.

Acknowledgements

Financial support for this work provided by members of the Cooling Technologies Research Center (CTRC), a graduated National Science Foundation (NSF) Industry/University Cooperative Research Center at Purdue University, and the National Science Foundation (grant No. CMMI-1554189 and CMMI-1634832) are gratefully acknowledged. The authors acknowledge Bojing Yao, Rishav Roy, Srivathsan Sudhakar, and Chen Chen for their assistance with the measurements and characterization.

References

[1] Marotta, E. E., and Hana, B., "Thermal Control of Interfaces for Microelectronic Packaging," *MRS Online Proceedings*, Library Archive 515 (1998).

[2] Atluri, V.P., Mahajan, R.V., Patel, P.R., Mallik, D., Tang, J., Wakharkar, V.S., Chrysler, G.M., Chiu, C.P., Choksi, G.N. and Viswanath, R.S., "Critical aspects of high-performance microprocessor packaging," *MRS Bulletin*, 28(1), pp.21-34 (2003).

[3] Garimella, S.V., Fleischer, A.S., Murthy, J.Y., Keshavarzi, A., Prasher, R., Patel, C., Bhavnani, S.H., Venkatasubramanian, R., Mahajan, R., Joshi, Y. and Sammakia, B., "Thermal challenges in next-generation electronic systems," *IEEE Transactions on Components and Packaging Technologies*, 31(4), pp.801-815 (2008).

[4] Prasher, R., "Thermal interface materials: historical perspective, status, and future directions," *Proceedings of the IEEE*, 94(8), pp.1571-1586 (2006).

[5] Cooper, M.G., Mikic, B.B. and Yovanovich, M.M., "Thermal contact conductance," *International Journal of Heat and Mass Transfer*, 12(3), pp.279-300 (1969).

[6] Madhusudana, C.V. and Ling, F.F., *Thermal Contact Conductance* (pp. 1-43), New York: Springer-Verlag (1996).

[7] Yeh, L.T. and Chu, R.C., *Thermal Management of Microelectronic Equipment*, New York: ASME (2002).

[8] Antonetti, V.W., and Yovanovich, M.M., "Enhancement of Thermal Contact Conductance by Metallic Coatings: Theory and Experiment," *Journal of Heat Transfer*, 107, no. 3: 513–19 (1985).

[9] Lambert, M.A. and Fletcher, L.S., "Review of the thermal contact conductance of junctions with metallic coatings and films," *Journal of Thermophysics and Heat Transfer*, 7(4) (1993).

[10] Merrill, C.T. and Garimella, S.V., "Measurement and prediction of thermal contact resistance across coated joints," *Experimental Heat Transfer*, 24(2), pp.179-200 (2011).

[11] Bar-Cohen, A., Matin, K. and Narumanchi, S., "Nanothermal interface materials: technology review and recent results," *Journal of Electronic Packaging*, 137(4), p.040803 (2015).

[12] McNamara, A.J., Joshi, Y. and Zhang, Z.M., "Characterization of nanostructured thermal interface materials–a review," *International Journal of Thermal Sciences*, 62, pp.2-11 (2012).

[13] Hansson, J., Nilsson, T.M., Ye, L. and Liu, J., "Novel nanostructured thermal interface materials: a review," *International Materials Reviews*, pp.1-24 (2017).

[14] Ishida, H. and Rimdusit, S., "Very High Thermal Conductivity Obtained by Boron Nitride-Filled Polybenzoxazine," *Thermochimica Acta*, 320, no. 1: 177–86 (1998).

[15] Lin, W., Moon K., and Wong, C.P., "A Combined Process of In Situ Functionalization and Microwave Treatment to Achieve Ultrasmall Thermal Expansion of Aligned Carbon Nanotube–Polymer Nanocomposites: Toward Applications as Thermal Interface Materials," *Advanced Materials,* 21, no. 23: 2421–24 (2009).

[16] Shahil, K.M.F., and Balandin, A.A., "Thermal Properties of Graphene and Multilayer Graphene: Applications in Thermal Interface Materials," *Solid State Communications*, Exploring Graphene, Recent Research Advances, 152, no. 15: 1331–40 (2012).

[17] Pashayi, K., Fard, H.R., Lai, F., Iruvanti, S., Plawsky, J., and Borca-Tasciuc, T., "Self-Constructed Tree-Shape High Thermal Conductivity Nanosilver Networks in Epoxy," *Nanoscale,* 6, no. 8: 4292–96 (2014).

[18] Iijima, S., "Helical microtubules of graphitic carbon," *Nature*, 354, pp.56-58 (1991).

[19] Marconnet, A.M., Panzer, M.A. and Goodson, K.E., "Thermal conduction phenomena in carbon nanotubes and related nanostructured materials," *Reviews of Modern Physics*, 85(3), p.1295 (2013).

[20] Wasniewski, J.R., Altman, D.H., Hodson, S.L., Fisher, T.S., Bulusu, A., Graham, S. and Cola, B.A., "Characterization of metallically bonded carbon nanotube-based thermal interface materials using a high accuracy 1D steady-state technique," *Journal of Electronic Packaging*, 134(2), p.020901 (2012).

[21] Lin, W., Zhang, R., Moon, K.S. and Wong, C.P., "Synthesis of high-quality vertically aligned carbon nanotubes on bulk copper substrate for thermal management," *IEEE Transactions on Advanced Packaging*, 33(2), pp.370-376 (2010).

[22] Shaddock, D., Weaver, S., Chasiotis, I., Shah, B. and Zhong, D., 2011. "Development of a compliant nanothermal interface material," *ASME InterPack,* IPACK2011-52015 (2011).

[23] Kempers, R., Lyons, A.M. and Robinson, A.J., "Modeling and experimental characterization of metal microtextured thermal interface materials," *Journal of Heat Transfer*, 136(1), p.011301 (2014).

[24] Feng, B., Faruque, F., Bao, P., Chien, A., Kumar, S., and Peterson, G. P., "Double-Sided Tin Nanowire Arrays for Advanced Thermal Interface Materials," *Applied Physics Letters,* 102, no. 9: 093105 (2013).

[25] Barako, M.T., Roy-Panzer, S., English, T.S., Kodama, T., Asheghi, M., Kenny, T.W. and Goodson, K.E., "Thermal Conduction in Vertically Aligned Copper Nanowire Arrays and Composites," *ACS Applied Materials & Interfaces*, 7, no. 34: 19251–59 (2015).

[26] *Implementation Agreement for Thermal Interface Specification for Pluggable Optics Modules,* Optical Internetworking Forum, OIF-Thermal-01.0, (2015).

[27] Cui, J., Wang, J., Zhong, Y., Pan, L., Weibel, J.A., "Metallized Compliant Three-Dimensional Microstructures for Dry Contact Thermal Conductance Enhancement," *Journal of Micromechanics and Microengineering* 28, no. 5: 055005 (2018).

[28] Wasielewski, R., Cui, J., Pan, L., Weibel, J. A., "Fabrication of Compliant Three-Dimensional Microstructures as Surface Coatings for Dry Contact Thermal Conductance Enhancement." *15th IEEE Intersociety Conference on Thermal and Thermomechanical Phenomena in Electronic Systems (ITherm)*, 134–39 (2016).

[29] Sun, C., Fang, N., Wu, D.M. and Zhang, X., "Projection micro-stereolithography using digital micro-mirror dynamic mask," *Sensors and Actuators A: Physical*, 121(1), pp.113-120 (2005).

[30] Zheng, X., Deotte, J., Alonso, M.P., Farquar, G.R., Weisgraber, T.H., Gemberling, S., Lee, H., Fang, N. and Spadaccini, C.M., "Design and optimization of a light-emitting diode projection micro-stereolithography three-dimensional manufacturing system," *Review of Scientific Instruments*, 83(12), p.125001 (2012).

[31] Bao, Y., He, C., Zhou, F., Stuart, C. and Sun, C., "A realistic design of three-dimensional full cloak at terahertz frequencies," *Applied Physics Letters*, 101(3), p.031910 (2012).

[32] Lin, D., Nian, Q., Deng, B., Jin, S., Hu, Y., Wang, W. and Cheng, G.J., "Three-dimensional printing of complex structures: man made or toward nature?" *ACS Nano*, 8(10), pp.9710-9715 (2014).

[33] Meza, L.R., Das, S. and Greer, J.R., "Strong, lightweight, and recoverable three-dimensional ceramic nanolattices," *Science*, 345(6202), pp.1322-1326 (2014).

[34] Soukoulis, C.M. and Wegener, M., "Past achievements and future challenges in the development of three-dimensional photonic metamaterials," *Nature Photonics*, 5(9), pp.523-530 (2011).

[35] Mallory, G.O., Hajdu, J.B., *Electroless plating: fundamentals and applications*, William Andrew, (1990).

[36] Lim, V. W. L., Kang, E. T., Neoh., K. G., "Electroless Plating of Palladium and Copper on Polypyrrole Films." *Synthetic Metals*, 123, no. 1: 107–15, (2001).